Reduced Graphene Oxide on Activated Carbon/Manganese Dioxide Composite Materials for High-Performance Supercapacitor Electrodes

Adinandra Caesar Fachrudin

Laboratory of Material Physics and Instrumentation, Department of Physics, Universitas Gadjah Mada, Yogyakarta, 55281, Indonesia https://orcid.org/0000-0002-9190-830X

Harsojo Sabarman (harsojougm@ugm.ac.id)

Laboratory of Material Physics and Instrumentation, Department of Physics, Universitas Gadjah Mada, Yogyakarta, 55281, Indonesia

Research Article

Keywords: Supercapacitor, Electrode, Activated Carbon, Manganese Dioxide, Reduced Graphene Oxide

Posted Date: February 7th, 2022

DOI: https://doi.org/10.21203/rs.3.rs-1319369/v3

Abstract

This study presents the addition of reduced graphene oxide (rGO) on the surface of activated carbon–manganese dioxide ($ACMnO_2$) composite material via high-temperature variations of 350 to 450 °C to increase the specific capacitance of the $ACMnO_2$/rGO composite electrode. The composite material is synthesized by coating the slurry mixture on the aluminum sheet using a 2-step doctor blade method with polyvinylidene difluoride (PVDF) material and dimethylformamide (DMF) solution as a binder. Then symmetric supercapacitor is fabricated using filter paper as a separator and 3M potassium hydroxide (KOH) solution as an electrolyte. The composite material analysis is characterized by X-ray diffraction (XRD) and scanning electron microscope (SEM) as well as cyclic voltammetry (CV) for the electrochemical properties. The $ACMnO_2$/rGO composite electrode at a temperature variation of 350 °C showed the highest specific capacitance of 459.79 F g^{-1} at a scan rate of 9 mV s^{-1} with an energy density of 63.859 Wh kg^{-1}. The addition of rGO on the surface of the $ACMnO_2$ composite material increased the specific capacitance by about 58% compared to without rGO, showing promises for high-performance supercapacitor electrodes.

Introduction

According to Enerdata, world energy consumption has increased by 58% in the last 30 years (1990 – 2020). The top three most widely used energy sources include oil (30%), coal (26%), and natural gas (24%), of which all three are fossil energy sources. The use of fossil energy sources has caused negative impacts on the environment, such as the greenhouse effect and global warming (U.S. EIA) result in the increase of atmospheric concentration and temperature of the earth's surface by 0.85 °C between 1800 to 2012 based on the assessments by the IPCC.

The solution to these problems in the context of scientists is through research on renewable and environmentally friendly energy sources and on energy storage systems. However, the main problem in research on renewable and environmentally friendly energy sources is the high cost due to the massive scale of the research. According to Europa Union, the total global investments for this research have always exceeded USD 200 billion since 2010. Moreover, the cost of electricity by these energy sources is still much higher than fossil energy sources. It makes renewable and environmentally friendly energy sources only contribute 10% of world energy consumption.

Energy storage system (ESS) refers to the device of converting electrical energy from power systems into a form that can be stored for converting back to electrical energy when needed [1]. Supercapacitors (SCs) is a new alternative ESS device that can combine electrochemical and electrostatic mechanisms, which result in higher specific power than batteries and higher specific energy than conventional capacitors. The main focus of research on the SCs is how to find electrode materials that can produce high performance.

Activated carbon (AC) is one of the carbon materials that can be obtained by two processes, including carbonization and activation from raw carbon resources. AC derived from coconut shells have advantages such as large carbon composition, high specific surface area, easily controlled pore structure, and low dust composition [2]. AC have specific surface area ranging from 300 to 3500 m^2 g^{-1} [3]. However, its maximum specific capacitance is low, usually below 200 F g^{-1}.

Composite materials from AC and nano transition metal oxide become an alternative because they can provide redox reactions [4]. Manganese dioxide (MnO_2) is widely used in the SCs because it serves fast and reversible redox reactions with theoretical specific capacitance up to 1370 F g^{-1} [5-6]. Furthermore, MnO_2 is abundant material in nature, low cost, non-toxic, and environmentally friendly [7]. AC and MnO_2 composite materials can be synthesized by deposition methods both solvothermal and hydrothermal [2, 8].

Reduced graphene oxide (rGO) is one of the graphene derivatives, which has a variety of unique optical, electrical, mechanical, and thermal properties [9]. Moreover, rGO can be synthesized by a method that is considered cheaper, simpler, and more efficient than graphene. The addition of rGO to composite materials from AC and MnO_2 had previously been done but obtained the specific capacitance of only 80 F g^{-1} because the mass percentage of 2% and the heating temperature of 100 °C is not enough to facilitate rGO effectively [10]. Therefore, in this study, the addition of rGO will use a large mass percentage through high heating temperatures. As expected, it will increase the mesopore and the adsorption capacity by ensuring rGO is on top of composite materials from AC and MnO_2.

Materials and Methods

Materials

AC was derived from coconut shell wastes with a specific capacitance of 80.9 F g^{-1}, a specific surface area of 1089 m^2 g^{-1}, and dominant pore distribution on micropores [2]. MnO_2 (Merck) had a grain size below 30 nm. rGO was synthesized by a modified Liquid-Phase Exfoliation (LPE) method with a heating temperature of 90 °C [11]. Moreover, polyvinylidene difluoride (PVDF) (Sigma-Aldrich) material and dimethylformamide (DMF) (Merck) solution were also used without any modification.

Synthesis Method of Composite Materials

AC (85%), MnO_2 (5%), and PVDF (10%) materials were mixed in a beaker glass by adding the DMF solution. Then the mixture was stirred (Cimarec Digital Hot Plate Stirrer 3067-20) using 200 rpm at 80 °C for 2 hours to reach a homogenous condition and slurry-like shape. Furthermore, the slurry mixture was coated on the aluminum sheet using the doctor blade method and then heated in a furnace at a temperature of 80 °C for 30 minutes.

rGO (90%) and PVDF (10%) materials were mixed in a beaker glass by adding the DMF solution. The ratio of total mass between the rGO mixture and the $ACMnO_2$ mixture was 1:1. Then the mixture was stirred using 200 rpm at 80 °C for 1 hour to reach a homogenous condition and slurry-like shape. Furthermore, the slurry mixture was coated on the aluminum sheet containing $ACMnO_2$ composite materials and then heated in a furnace at various heating temperatures of 350 °C, 400 °C, and 450 °C for 1 hour.

Fabrication Method of Supercapacitors

The components of SCs include filter paper as a separator and 3 M potassium hydroxide (KOH) solution as an electrolyte. $ACMnO_2$ and $ACMnO_2$/rGO composite materials were used as electrodes with approximately 1.5 × 1.5 cm in size, 0.3 mm in thickness, and 0.005 g in mass. Then the back of the electrodes was glued to copper tape as a current collector. Symmetrical SCs were fabricated in two acrylics with screws to press all the components of SCs inside them.

Characterization Method

Specific capacitance and energy density of the SCs were measured by cyclic voltammetry (CV) (Keithley 2400-C) measurements using data acquisition software from [12] at a voltage of 0 to 1 V with a scan rate of 9 mV s^{-1}. Both samples with rGO that have the highest specific capacitance and a sample without rGO will be further characterized by X-ray diffraction (XRD) and scanning electron microscope (SEM)). The lattice constants and crystallite size of composite materials were obtained by XRD (Rigaku MiniFlex 600) using copper X-rays spectrum at an angle of 10° to 80° at a rate of 0.02° min^{-1}. Distribution of the smallest size and the constituent elements and the surface morphology of composite materials were obtained by SEM (JEOL JSM-6510 LA) on

the cross-sectional images using EDX and Mapping working parameters at a voltage of 10 kV with energy ranging from 0 to 20 keV.

Results and Discussion

The CV curve in Figure 1 shows a non-square shape and a small peak at the end of the charging/discharging process because of the type of material used in the electrodes. Carbon material (AC, rGO) involves the adsorption/desorption process of ions from the electrolyte in its pores (non-faradaic), causing the CV curve to widen. Meanwhile, nano transition metal oxide (MnO_2) involves the reduction/oxidation process with the electrolyte (faradaic), causing redox peaks. Characteristics of the redox peaks in all samples did not change, indicating that the high heating temperature did not affect the crystal structure of MnO_2. However, the redox peak in the ACMnO2/rGO-450 sample is lower than the other samples with rGO, indicating that the heating temperature above 400 °C decreased the pseudocapacitance mechanism.

The heating temperature of rGO above 300 °C resulted in the loss of water intercalation/deintercalation process, removal of more stable oxygen functional groups, and increased ion adsorption/desorption capacity up to 40 times [13]. However, it started to decrease when it reached a heating temperature of 500 °C. In addition, the heating temperature between 300 °C and 400 °C increased the mesopore, achieved better cycle stability, and presented a carbonyl functional group C=O [14]. In contrast to other carbonyl functional groups such as C-O-C, and O=C-O, which adversely affect the conductivity and specific surface area of rGO, C=O contributes to the pseudocapacitance mechanism.

Specific capacitance (C_s) in F g^{-1} and energy density (E_s) in Wh kg^{-1} are given by Equation 1 and 2 as follows:

$$C_s = \frac{\int i\, dV}{S\, m\, V} \tag{1}$$

$$E_s = \frac{1}{2}\frac{C_s V^2}{3.6} \tag{2}$$

in which $\int i\, dV$ (A V) is the area of the CV curve, S (mV s^{-1}) is scan rate, m (g) is the mass of the electrode materials, and V (V) is voltage. Therefore, the larger the CV curve formed, the greater the specific capacitance and energy density obtained. As shown in Table 1, the ACMnO2/rGO-350 sample has the highest specific capacitance compared to the other samples with rGO, which unexpectedly decreased specific capacitance. The addition of rGO on the $ACMnO_2$ sample increased the specific capacitance up to 58% compared to without rGO. Hence, the effect of high heating temperature in the addition of rGO to specific capacitance is nonlinear. However, this research cannot provide the effectiveness of the redox reaction of MnO_2 to specific capacitance or specific surface area.

The XRD patterns in Figure 2 fitted in using Origin 2021 software to reduce noise and assist in determining the diffraction angle and FWHM (Full Width at Half Maximum). Both XRD patterns show narrow diffraction peaks with high intensity, indicating high crystallinity of the compounds contained in the $ACMnO_2$ and ACMnO2/rGO composite materials. Meanwhile, the interplanar spacing (d) between adjacent lattice planes is given by Bragg's equation as follows:

$$d = \frac{\lambda}{2 \sin\theta} \tag{3}$$

in which λ is the X-rays wavelength, and θ is the diffraction angle. The lattice constants (a, c) depend on the crystal structure, where MnO_2 has a tetragonal crystal structure while graphite has a hexagonal crystal structure. So, the lattice constants are explicitly given by Equation 4 and 5 as follows:

Tetragonal $\rightarrow \frac{1}{d^2} = \frac{h^2+k^2}{a^2} + \frac{l^2}{c^2}$ (4)

Hexagonal $\rightarrow \frac{1}{d^2} = \frac{4}{3}\frac{(h^2+k^2+hk)}{a^2} + \frac{l^2}{c^2}$ (5)

in which hkl is Miller indices from lattice planes of crystal structure.

The XRD pattern of the $ACMnO_2$ sample in Figure 2a shows diffraction peaks at angles of 44.093°, 64.565°, and 77.745°, corresponding to graphite (101) and α-MnO_2 (321, 002, 332). The lattice constants shown in Table 2 show that AC has lattice constants close to a = 2.456 Å and c = 6.696 Å from graphite (JCPDS 41-1487). Meanwhile, MnO_2 has lattice constants close to a = 9.920 Å and c = 2.925 Å from α-MnO_2 (JCPDS 44-0141). The use of α-MnO_2 is due to larger pore size than other MnO_2 or other nano transition metal oxide, which supports the ions adsorption/desorption process [15]. The XRD pattern of the $ACMnO_2$/rGO sample in Figure 2b shows diffraction peaks at angles of 26.255°, 44.442°, 64.854°, and 78.009°, corresponding to graphite (002, 101) and α-MnO_2 (321, 002, 332). The lattice constants shown in Table 3 show that AC and rGO also have lattice constants close to graphite, and MnO_2 has lattice constants close to α-MnO_2.

The addition of rGO causes a diffraction peak at the 002 graphite plane to be the most dominant, which previously disappeared. Moreover, the intensity of diffraction peak at the angle of 44.442° corresponding to two compounds increase. The diffraction peaks of all compounds still appear and do not shift significantly, indicating that there is no reaction between all materials. Therefore, the properties of composite materials are a combination of the physical and chemical properties of each constituent material. Meanwhile, the crystallite size (D) is given by Scherrer's equation as follows:

$$D = \frac{K\,\lambda}{\beta\,\cos\theta} \quad (6)$$

in which K is the dimensionless shape factor, which has a typical value of about 0.9, and β is FWHM. The results shown in Table 4 and Table 5 shows that the $ACMnO_2$ sample has an average crystallite size of $\overline{D}$ = 18.0 ± 0.8 nm, and the $ACMnO_2$/rGO sample has an average crystallite size of $\overline{D}$ = 18 ± 3 nm.

AC and MnO_2 only have interfaces bonding and are uncompounded [2]. Therefore, MnO_2 only has a reaction with ions from the electrolyte, which can be written as follows:

$$MnO_2 + K^+ + e^- \rightleftarrows MnO_2K \quad (7)$$

$$(MnO_2)_{surface} + K^+ + e^- \rightleftarrows (MnO_2{}^-K^+)_{surface} \quad (8)$$

in which the oxidation states of Mn will change from +4 on MnO_2 to +3 on MnO_2K and $MnO_2{}^-K^+$. Eq. 7 shows the process of intercalation/deintercalation of cations on the inside of MnO_2 when the redox process takes place. This process does not change the crystal structure of MnO_2. Meanwhile, Eq. 8 shows the process of adsorption/desorption of ions on the surface of MnO_2, but with a smaller amount than adsorption/desorption of ions on the carbon pores. The two equations show that cations have an important role in the performance of SCs.

The presence of fast and reversible redox reactions requires an electrolyte with high conductivity and mobility. Therefore, the use of the aqueous electrolyte is more appropriate than the organic or ionic electrolyte. KOH electrolyte used in this research is an aqueous electrolyte. Each ion has a radius of 0.138 nm for K^+ and 0.110 nm for OH^- [16]. Small ion size supports the large number of ions that can get into carbon pores. The K^+ ion has a conductivity of 73 $cm^2\ \Omega^{-1}\ mol^{-1}$ and mobility of $7.62 \times 10^{-4}\ cm^2\ V^{-1}$, which is higher than other cations such as

Na^+ and Li^+ [17]. Meanwhile, the OH^- ion has a conductivity of 198 $cm^2\ \Omega^{-1}\ mol^{-1}$ and mobility of 20.64×10^{-4} $cm^2\ V^{-1}$, which is higher than other anions such as Cl^- and $SO_4{}^{2-}$ [18].

Cross-sectional SEM images in Figure 3 show that the addition of rGO through high heating temperature broke the surface of composite materials into smaller and more equal sizes, resulting in the surface morphology being more homogenous. The smallest size average and distribution are obtained by using ImageJ and Origin 2021 software. The curve is shown as an inset in Figure 3a and 3b, which show a decrease after the addition of rGO. EDX test for the $ACMnO_2$ sample in Figure 4a shows the mass percentage of carbon, oxygen, and manganese elements are 86.99%, 12.27%, and 0.74%, respectively. This number is close to the proportion of material used in the synthesis of $ACMnO_2$ composite materials. It also shows that the binder used is eliminated in the synthesis process, where PVDF material and DMF solution contain other elements such as hydrogen, fluorine, and nitrogen.

EDX test in Figure 4b also shows that the addition of rGO increased the mass and atomic percentage of the oxygen element by 82% and 86%, respectively but decreased the mass and atomic percentage of the carbon element by 11% and 9%, respectively. It indicates that the rGO used still has several stable oxygen functional groups which are not disappearing at the heating temperature of 350 °C. Meanwhile, the manganese element only has a small mass and atomic percentage, indicating the pseudocapacitance mechanism of MnO_2 has less contribution than the EDL mechanism of carbon. Mapping tests also support the result of EDX tests. As shown in Figure 5, the carbon element marked with red was dominant before the addition of rGO. However, after the rGO was added, the oxygen element marked with green was significantly increased on the surface morphology of the composite materials. Therefore, the method used in this research successfully ensured the rGO on top of the $ACMnO_2$ surface.

Conclusion

The addition of rGO on the surface of the $ACMnO_2$ composite material was achieved successfully by high heating temperature, where rGO decreased the smallest size average and distribution, increased the mass and atomic percentage of the oxygen element but did not cause the reaction with either AC or MnO_2. The SCs of the $ACMnO_2$/rGO composite electrode at a temperature variation of 350 °C obtained the highest specific capacitance of 459.79 F g^{-1} at a scan rate of 9 mV s^{-1}, where the addition of rGO increased the specific capacitance by about 58% compared to without rGO.

For further research, it is still necessary to add other characterization methods such as DSC (Differential Scanning Calorimetry), BET (Brunauer-Emmett-Teller), and TEM (Transmission Electron Microscope) for the $ACMnO_2$/rGO composite electrode as well as GC (Galvanostatic Cycling) and EIS (Electrochemical Impedance Spectroscopy) for the SCs. Furthermore, variations can also be made on the SCs components such as a binder, separator, and electrolyte to make the SCs with different characteristics both in performance and flexibility.

Acknowledgments

The authors would like to thank Haris Suhendar, M.Sc. and Buky Wahyu Pramata, M.Sc. from Universitas Gadjah Mada for helping the synthesis and characterization process. This study was supported by grant from Hibah Penelitian BOPTN FMIPA Universitas Gadjah Mada.

References

[1] Wang Y, Xu Y, Qiu J (2020) Distributed finite-time control of aggregated energy storage sytems for frequency regulation in multiarea microgrids. In: Meng W, Wang X, Liu S (ed) Distributed control methods and cyber security issues in microgrids. Academic Press, Cambridge, pp 149-176.

[2] Doloksaribu ME (2019) Fabrication and characterization of supercapacitor based on nanopore activated carbon and transition metal oxide. Dissertation, Faculty of Mathematics and Natural Sciences, Universitas Gadjah Mada, Yogyakarta, 55281, Indonesia. http://etd.repository.ugm.ac.id/penelitian/detail/172082

[3] Vangari M, Pryor T, Jiang L (2013) Supercapacitors: review of materials and fabrication methods. Journal of Energy Engineering 139:72-79. https://doi.org/10.1061/(ASCE)EY.1943-7897.0000102

[4] Borenstein A, Hanna O, Attias R, Luski S, Brousse T, Aurbach D (2017) Carbon-based composite materials for supercapacitor electrodes: a review. Journal of Materials Chemistry A 5:12653-12672. https://doi.org/10.1039/C7TA00863E

[5] Wang Y, Guo J, Wang T, Shao J, Wang D, Yang WY (2015) Mesoporous transition metal oxides for supercapacitors. Nanomaterials 5:1667-1689. https://doi.org/10.3390/nano5041667

[6] Julien C, Mauger A, Vijh A, Zaghib K (2016) Lithium batteries. In: Julien C, Mauger A, Vijh, A, Zaghib K (ed) Lithium batteries. Springer International Publishing, Cham, pp 29-68.

[7] Julien CM, Mauger A (2017) Nanostructured MnO_2 as electrode materials for energy storage. Nanomaterials 7:396. https://doi.org/10.3390/nano7110396

[8] Shen H, Zhang Y, Song X, Liu Y, Wang H, Duan H, Kong X (2019) Facile hydrothermal synthesis of actiniaria-shaped α-MnO_2/activated carbon and its electrochemical performances of supercapacitor. Journal of Alloys and Compounds 770:926-933. https://doi.org/10.1016/j.jallcom.2018.08.228

[9] Kavitha C (2021) A review on reduced graphene oxide hybrid nano composites and their prominent applications. Materials Today: Proceedings. https://doi.org/10.1016/j.matpr.2021.05.343

[10] Harsojo, Doloksaribu M, Prihandoko B, Priyono S, Subhan A, Lestariningsih T (2019) The effect of reduced graphene oxide on the activated carbon metal oxide supercapacitor. Materials Today: Proceedings 13:181-186. https://doi.org/10.1016/j.matpr.2019.03.211

[11] Pratama BW, Dwandaru WSB (2020) Synthesis of reduced graphene oxide based on thermally modified liquid-phase exfoliation. Nano Express 1:010023. https://doi.org/10.1088/2632-959X/ab8685

[12] Suhendar H (2020) Ion separation using polyacrylonitrile (pan)/graphene oxide (go) based electrode in capacitive deionization (cdi) system. Thesis, Faculty of Mathematics and Natural Sciences, Universitas Gadjah Mada, Yogyakarta, 55281, Indonesia. http://etd.repository.ugm.ac.id/penelitian/detail/182526

[13] Dolbin AV, Khlistyuck MV, Esel'son VB, Gavrilko VG, Vinnikov NA, Basnukaeva RM, Maluenda I, Maser WK, Benito AM (2016) The effect of the thermal reduction temperature on the structure and sorption capacity of reduced graphene oxide materials. Applied Surface Science 361:213-220. https://doi.org/10.1016/j.apsusc.2015.11.167

[14] Liu Z, Diao Z, Yuan Y, Jia H, Wang L, Fei W (2021) A two-step thermal treatment method to produce reduced graphene oxide with selectively increasing electrochemically active carbonyl group content for high-performance supercapacitor electrode. Colloids and Surfaces A: Physicochemical and Engineering Aspects 620:126573. https://doi.org/10.1016/j.colsurfa.2021.126573

[15] Devaraj S, Munichandraiah N (2008) Effect of crystallographic structure of MnO_2 on its electrochemical capacitance properties. The Journal of Physical Chemistry C 112:4406-4417. https://doi.org/10.1021/jp7108785

[16] Pal B, Yang S, Ramesh S, Thangadurai V, Jose R (2019) Electrolyte selection for supercapacitive devices: a critical review. Nanoscale Advances 1:3807-3835. https://doi.org/10.1039/C9NA00374F

[17] Nithya VD, Selvan RK, Kalpana D, Vasylechko L, Sanjeeviraja C (2013) Synthesis of Bi_2WO_6 nanoparticle and its electrochemical properties in different electrolytes for pseudocapacitor electrodes. Electrochimica Acta 109:720-731. https://doi.org/10.1016/j.electacta.2013.07.138

[18] Wu H, Wang X, Jiang L, Wu C, Zhao Q, Liu X, Hu B, Yi L (2013) The effects of electrolyte on the supercapacitive performance of activated calcium carbide-derived carbon. Journal of Power Sources 226:202-209. https://doi.org/10.1016/j.jpowsour.2012.11.014

Table

Table 1 Specific capacitance and energy density of all samples

Sample	C_S (F g^{-1})	E_D (Wh kg^{-1})
$ACMnO_2$	291.78	40.525
$ACMnO_2$/rGO-350	459.79	63.859
$ACMnO_2$/rGO-400	267.08	37.094
$ACMnO_2$/rGO-450	233.45	32.424

Table 2 Lattice constants of $ACMnO_2$ sample

Peak	2θ	JCPDS		Strain	d (Å)	a (Å)	c (Å)
		2θ	hkl				
1	44.093	44.079	101	0.0003	2.053	2.487	6.785
		45.221	321	0.0249	2.053		
2	64.565	63.582	002	0.0155	1.443	9.919	2.885
3	77.745	76.836	332	0.0118	1.228		

Table 3 Lattice constants of $ACMnO_2$/rGO sample

Peak	2θ	JCPDS		Strain	d (Å)	a (Å)	c (Å)
		2θ	hkl				
1	26.255	26.610	002	0.0133	3.390	2.466	6.785
2	44.442	44.079	101	0.0082	2.037		
		45.221	321	0.0172	2.037		
3	64.854	63.582	002	0.0200	1.437	9.920	2.874
4	78.009	76.836	332	0.0153	1.224		

Table 4 Crystallite size of $ACMnO_2$ sample

Peak	2θ	β	D (nm)
1	44.093	0.504	17.004
2	64.565	0.523	17.963
3	77.745	0.540	18.884

Table 5 Crystallite size of $ACMnO_2$/rGO sample

Peak	2θ	β	D (nm)
1	26.255	0.570	14.307
2	44.442	0.501	17.140
3	64.854	0.488	19.287
4	78.009	0.484	21.116

Figure

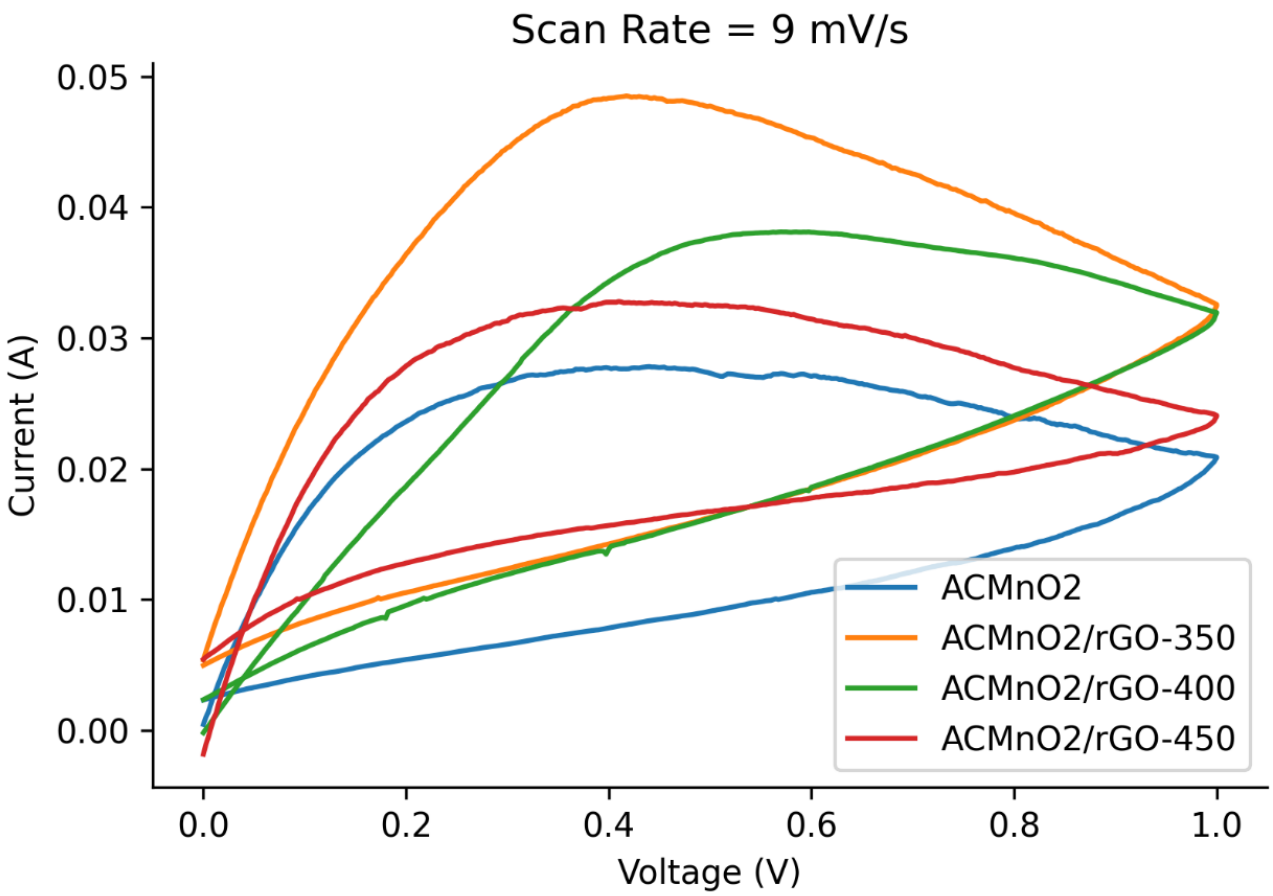

Figure 1 The CV Curve of all samples

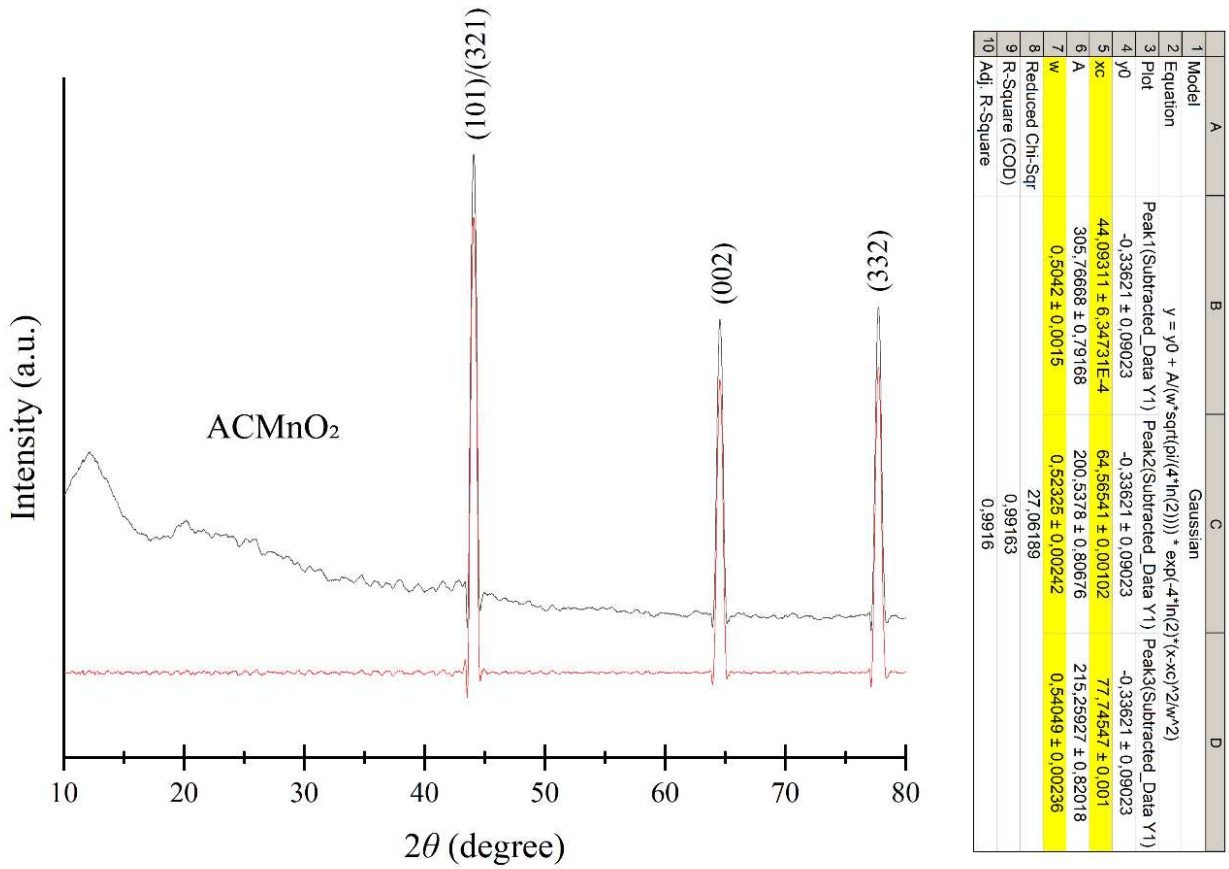

	A	B	C	D
1	Model	Gaussian		
2	Equation	y = y0 + A/(w*sqrt(pi/(4*ln(2)))) * exp(-4*ln(2)*(x-xc)^2/w^2)		
3	Plot	Peak1(Subtracted_Data Y1)	Peak2(Subtracted_Data Y1)	Peak3(Subtracted_Data Y1)
4	y0	-0,33621 ± 0,09023	-0,33621 ± 0,09023	-0,33621 ± 0,09023
5	xc	44,09311 ± 6,34731E-4	64,56541 ± 0,00102	77,74547 ± 0,001
6	A	305,76668 ± 0,79168	200,5378 ± 0,80676	215,25927 ± 0,82018
7	w	0,5042 ± 0,0015	0,52325 ± 0,00242	0,54049 ± 0,00236
8	Reduced Chi-Sqr	27,06189		
9	R-Square (COD)	0,99163		
10	Adj. R-Square	0,9916		

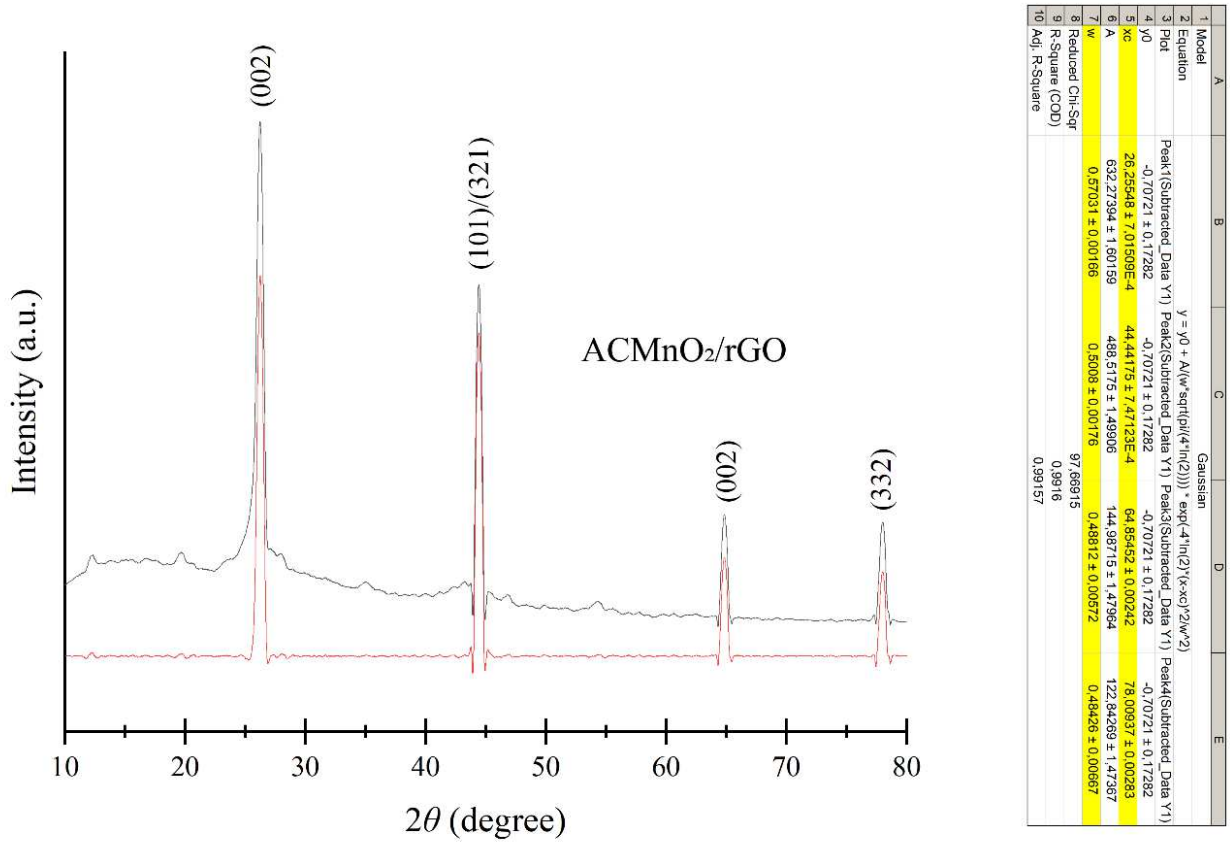

	A	B	C	D	E
1	Model	Gaussian			
2	Equation	y = y0 + A/(w*sqrt(pi/(4*ln(2)))) * exp(-4*ln(2)*(x-xc)^2/w^2)			
3	Plot	Peak1(Subtracted_Data Y1)	Peak2(Subtracted_Data Y1)	Peak3(Subtracted_Data Y1)	Peak4(Subtracted_Data Y1)
4	y0	-0,70721 ± 0,17282	-0,70721 ± 0,17282	-0,70721 ± 0,17282	-0,70721 ± 0,17282
5	xc	26,25548 ± 7,01509E-4	44,44175 ± 7,47123E-4	64,85452 ± 0,00242	78,00937 ± 0,00283
6	A	632,27394 ± 1,60159	488,5175 ± 1,49906	144,98715 ± 1,47984	122,84269 ± 1,47367
7	w	0,57031 ± 0,00166	0,5008 ± 0,00176	0,48812 ± 0,00572	0,48426 ± 0,00867
8	Reduced Chi-Sqr	97,66915			
9	R-Square (COD)	0,9916			
10	Adj. R-Square	0,99157			

Figure 2 The XRD pattern of (a) $ACMnO_2$ and (b) $ACMnO_2$/rGO samples

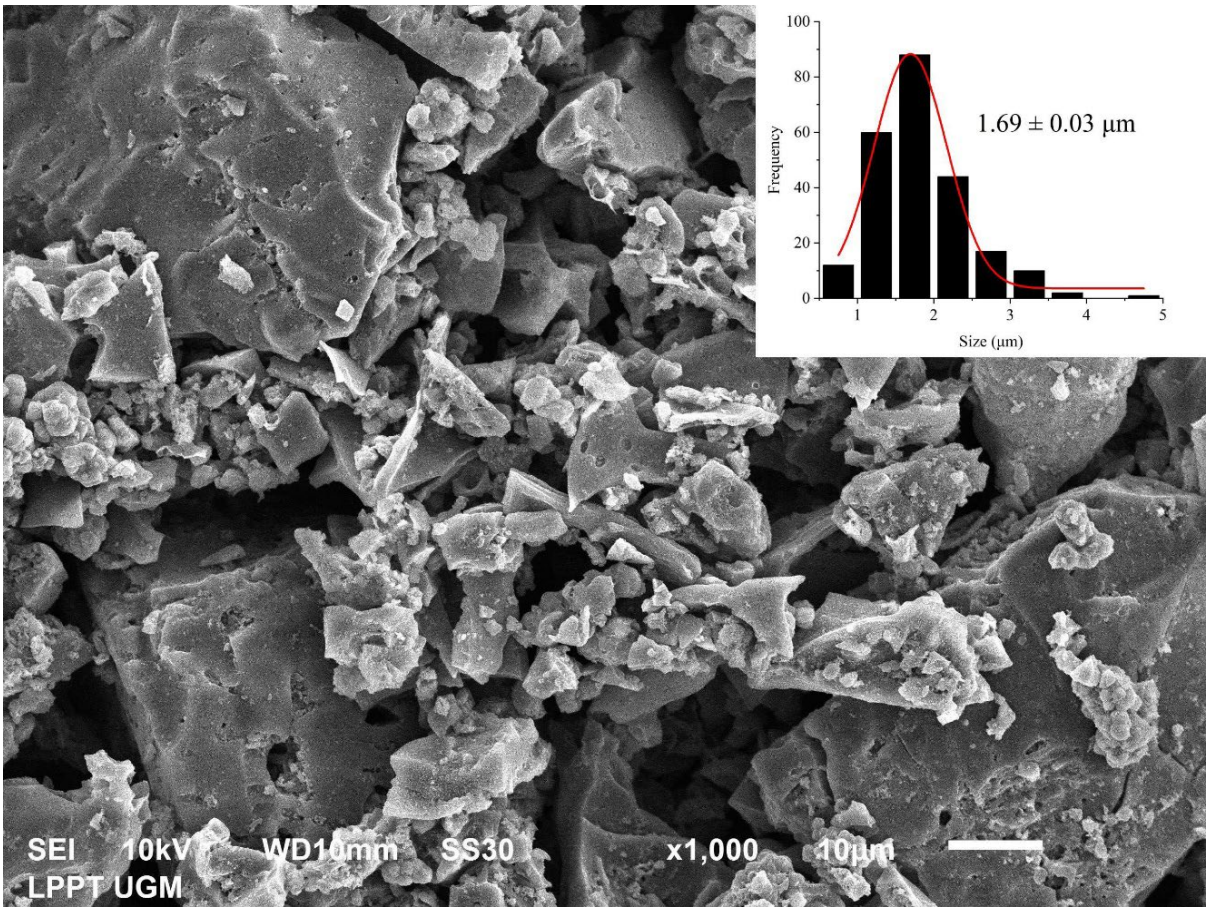

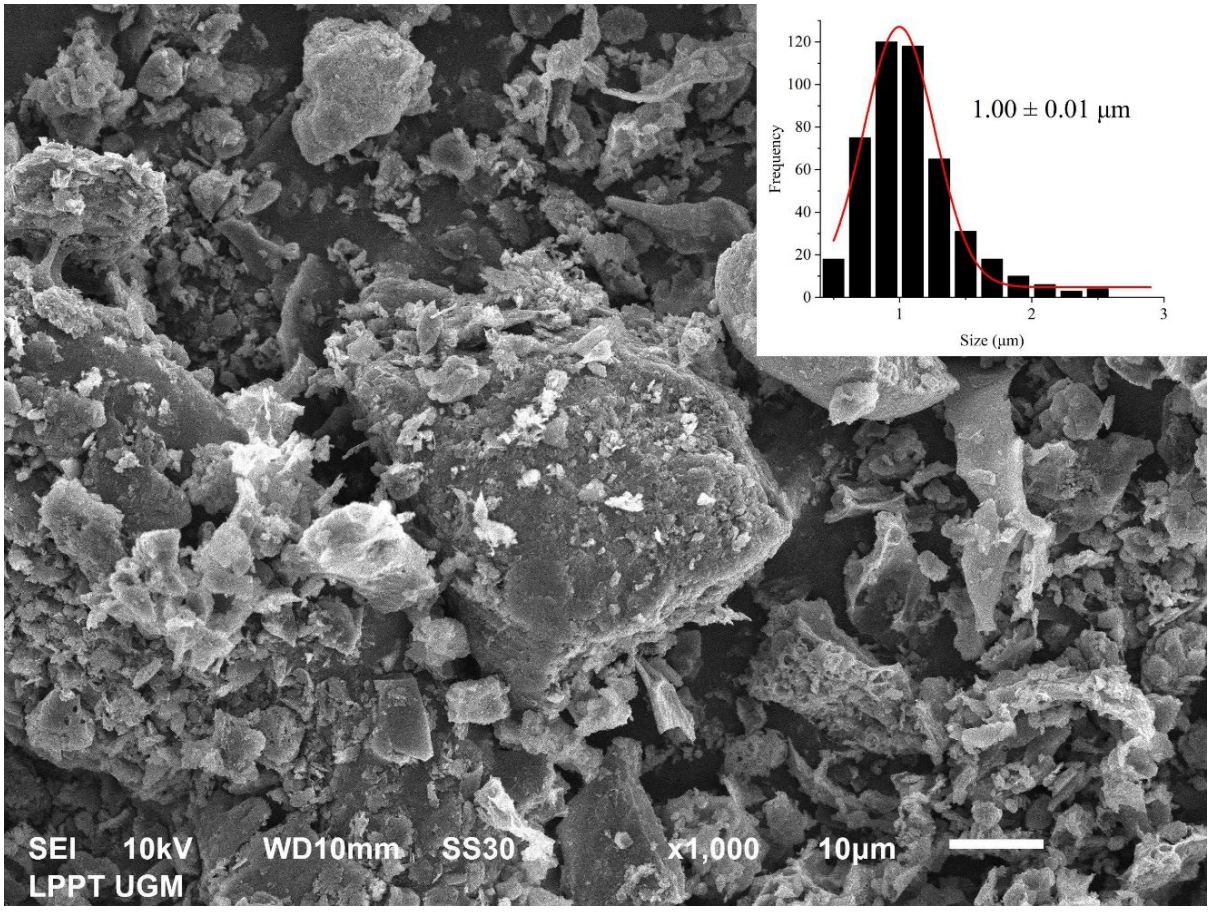

Figure 3 Cross-sectional SEM image of (a) $ACMnO_2$ and (b) $ACMnO_2$/rGO samples

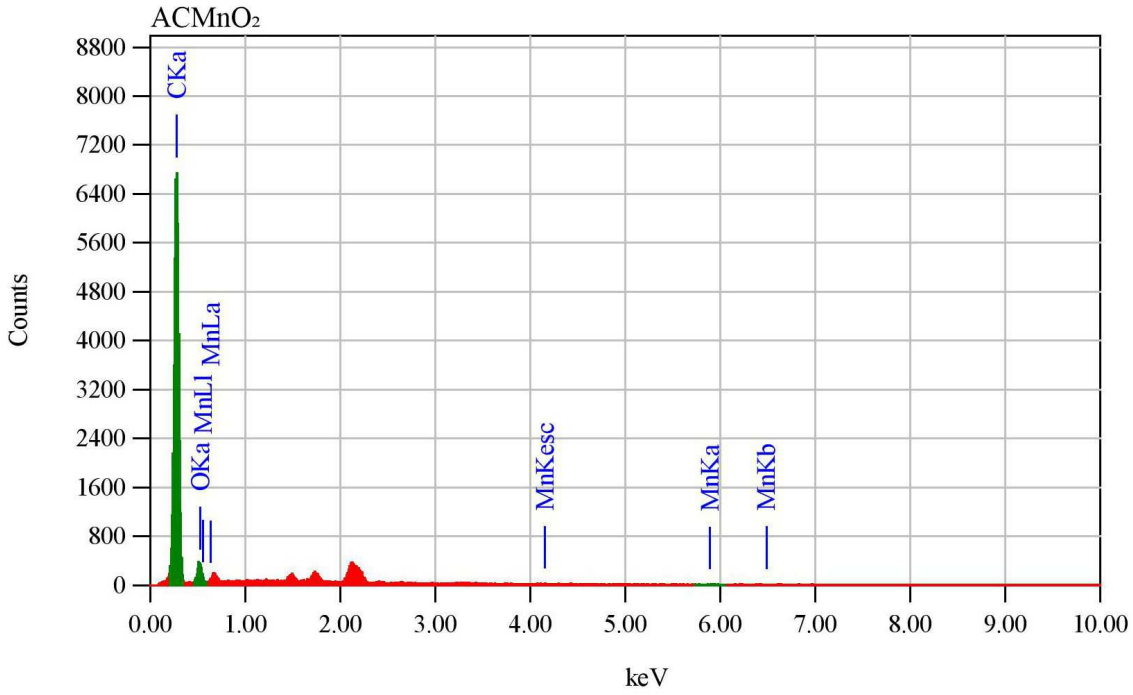

ZAF Method Standardless Quantitative Analysis
Fitting Coefficient : 0.1219

Element	(keV)	Mass%	Sigma	Atom%	Compound	Mass%	Cation	K
C K	0.277	86.99	0.21	90.27				92.0467
O K	0.525	12.27	0.24	9.56				7.2756
Mn K*	5.894	0.74	0.21	0.17				0.6778
Total		100.00		100.00				

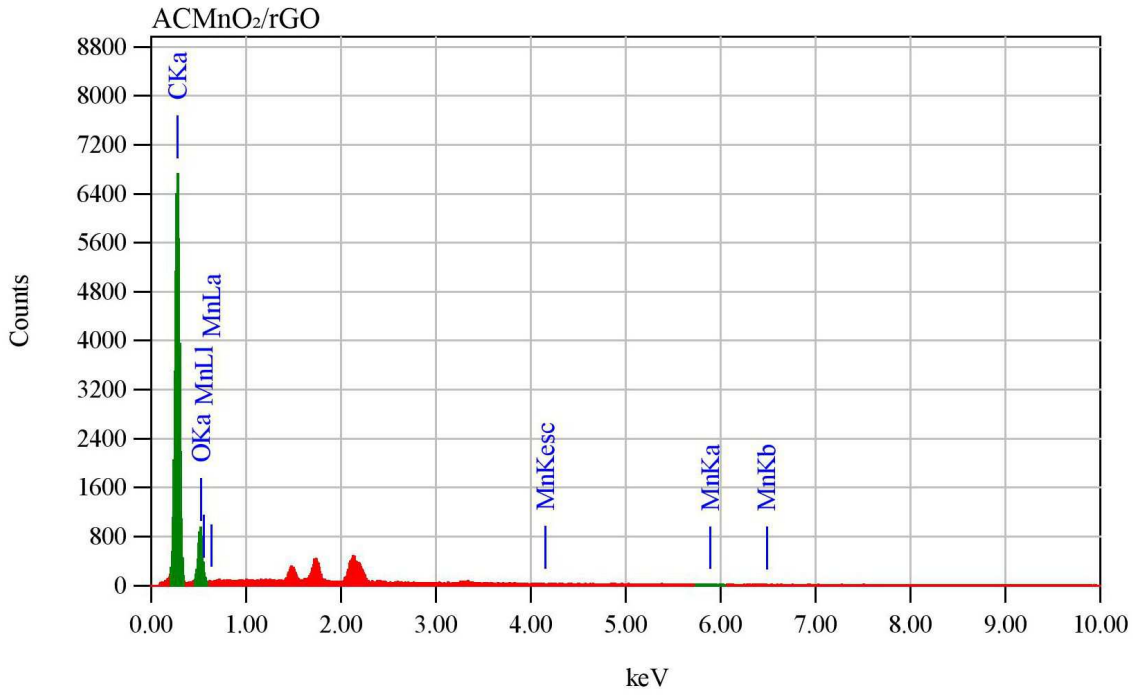

ZAF Method Standardless Quantitative Analysis
Fitting Coefficient : 0.1409

Element	(keV)	Mass%	Sigma	Atom%	Compound	Mass%	Cation	K
C K	0.277	77.27	0.19	82.10				83.7359
O K	0.525	22.33	0.28	17.81				15.8715
Mn K	5.894	0.40	0.20	0.09				0.3925
Total		100.00		100.00				

Figure 4 EDX test of (a) $ACMnO_2$ and (b) $ACMnO_2$/rGO samples

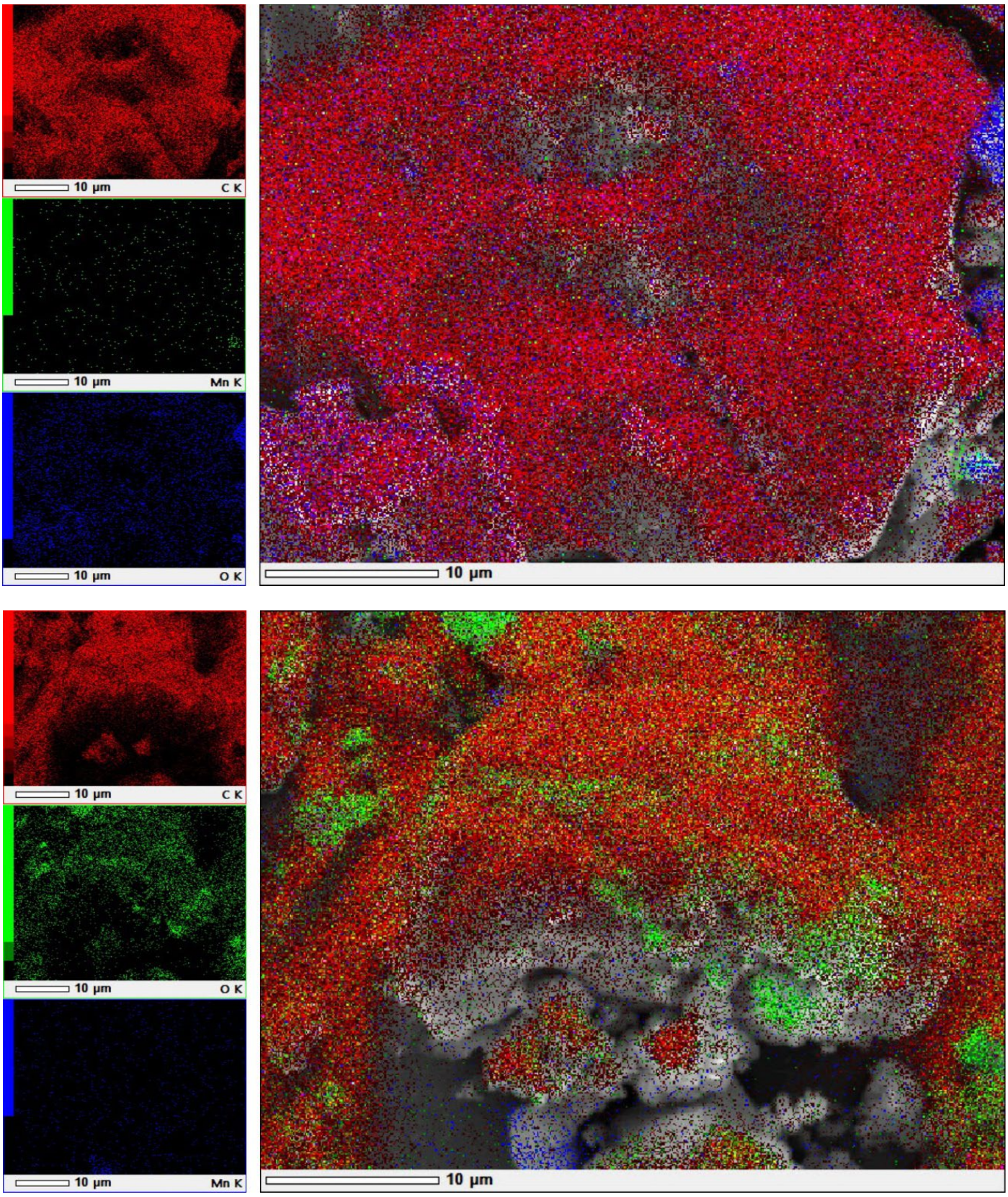

Figure 5 Mapping test of (a) $ACMnO_2$ and (b) $ACMnO_2$/rGO samples